Forecasting search areas using ensemble ocean circulation modeling

A. Melsom · F. Counillon · J. H. LaCasce · L. Bertino

Abstract We investigate trajectory forecasting as an application of ocean circulation ensemble modeling. The ensemble simulations are performed weekly, starting with assimilation of data for various variables from multiple sensors on a range of observational platforms. The ensemble is constructed from 100 members, and member no. 1 is designed as a standard (deterministic) simulation, providing us with a benchmark for the study.

We demonstrate the value of the ensemble approach by validating simulated trajectories using data from ocean surface drifting buoys. We find that the ensemble average trajectories are generally closer to the observed trajectories than the corresponding results from a deterministic forecast.

We also investigate an alternative model in which velocity perturbations are added to the deterministic results, and ensemble mean results, by a first-order stochastic process. The parameters of the stochastic model are tuned to match the dispersion of the ensemble approach. Search areas from the stochastic model give a higher hit ratio of the observations than the results based on the ensemble. However, we find that this is a consequence of a positive skew of the area distribution of the convex hulls of the ensemble trajectory end points.

Keywords Model validation · Lagrangian forecasts · Ensemble simulations · Ocean modeling · Search and rescue

1 Introduction

Operational trajectory forecasting for search and rescue operations is routinely performed using results for ocean currents from a single, deterministic ocean circulation forecast. In the present study, we compare this approach to one employing an ensemble model/assimilation system.

Ensemble data assimilation techniques were first proposed in the oceanographic context by Evensen (1994). Uncertainty estimates are propagated forward in time combining optimally the model and observations. These techniques also present a convenient framework for ensemble forecasting, as the same ensemble can be used consistently for data assimilation and probabilistic forecasting.

For this study, we apply the advanced assimilative ensemble model TOPAZ with which observations of temperature, salinity, sea level, sea ice concentration, and ice drift are assimilated by an ensemble Kalman filter (Bertino and Lisæter, 2008). The analysis, which is presently performed weekly, is followed by a 7-day ensemble forecast using 100 members. This is the operational model system for real-time ocean forecasting

A. Melsom
Norwegian Meteorological Institute, P.O. Box 43 Blindern,
NO-0313 Oslo, Norway.
E-mail: arne.melsom@met.no

F. Counillon
Mohn Sverdrup Center / Nansen Environmental and Remote
Sensing Center, Bergen, Norway

J. H. LaCasce
Department of Geosciences, University of Oslo, Oslo, Norway

L. Bertino
Mohn Sverdrup Center / Nansen Environmental and Remote
Sensing Center, Bergen, Norway

in MyOcean's Arctic Monitoring and Forecasting Centre.[1] Products and services for marine safety and for the coastal and marine environment are at the heart of MyOcean.

In the present study, we evaluate a definition of impact (search) areas that is derived from the spread of trajectories in the ensemble results. Then, we compare the information available from a large model ensemble with the deterministic (one member) case. Quantifications are obtained by comparing the final position of the trajectories from model results with corresponding data from ocean surface drifting buoys.

Forecasting of drifting objects is performed operationally with information about winds, waves, ocean currents, and properties of the drifting object (Hackett et al., 2006; Breivik and Allen, 2008). The resulting drift trajectories are generally deflected from the ambient ocean currents. This relative motion is commonly known as the object's "leeway" (Allen and Plourde, 1999; Breivik et al., 2011). However, the drifting buoys used in the study are attached to a drogue at 15 m depth and as such are only modestly affected by the actions of winds and waves. Thus, we will focus on the drift component that can be solely attributed to ocean currents.

The search area will be defined using the "convex hull" of trajectory end points starting from a known position of particle seeding. From earlier work using another approach for generating an ensemble, we know that the ensemble spread can be smaller than expected from observations (Melsom, 2010). In the present context of surface drift, processes that are not resolved by the circulation model may give rise to a low ensemble spread. Hence, we supplement our ensemble approach with results from a first-order stochastic model.

Section 2 presents the assimilation and ocean circulation model. Then, the observational platform of drifting buoys that are used as "truth" is described in Section 3. The validation follows in Section 4, along with a description of the stochastic model. The results are discussed, and our recommendations are given in Section 5.

2 The TOPAZ model

TOPAZ is a coupled ocean – sea ice data assimilation system developed for the North Atlantic Ocean, the Nordic Seas, the Arctic Ocean, and adjacent shelf seas. It is the main production system of the Arctic Marine Forecasting Center of the MyOcean project (`http://`

`www.myocean.eu.org`) and is used both for short-term forecasting and reanalysis purposes. For the present study, we use the latest version (TOPAZ 4, Sakov et al., 2012) which builds on TOPAZ 3 (Bertino and Lisæter, 2008). The model consists of the hybrid coordinate ocean model (HYCOM, Bleck, 2002; Chassignet et al., 2006) v. 2.2 coupled with a sea ice model (Hunke and Dukowicz, 1997). The system assimilates observations with the ensemble Kalman filter (Evensen, 1994; Evensen, 2003).

The present implementation of TOPAZ is run in a weekly cycle, starting with an assimilation step that is described in detail in Section 2.2 below. Model fields are subsequently integrated 1 week forward from the time of the analysis with HYCOM, which is described in Section 2.1. The initialization is performed for a date that precedes the wall clock by 1 week, allowing us to perform the integration based on a set of homogeneous atmospheric forcing fields. Details about the atmospheric forcing are presented in Section 2.3 below.

The model code is publicly available. It can be accessed from `https://svn.nersc.no/repos/hycom` or browsed at `https://svn.nersc.no/hycom/browser`.

2.1 Ocean model

In the present implementation, z-coordinates are used in the unstratified surface mixed layer, with a transition to isopycnal coordinates in the stratified ocean below. Isopycnal layers permit high resolution in areas of strong density gradients and better conservation of tracers and potential vorticity, whereas *z-layers* are well suited to regions where surface mixing is important. The tracer and continuity equations are solved with the second order flux corrected transport scheme (FCT2, Iskandarani et al., 2005; Zalesak, 1979), the turbulent mixing sub-model from the Goddard Institute for Space Studies (Canuto et al., 2002) is applied. Fixed and nonisopycnal coordinate layers are re-mapped in the vertical with the weighted essentially nonoscillatory piecewise parabolic scheme, and biharmonic viscosity is applied.

The grid has 880×800 horizontal grid points, with a variable grid spacing of 12 – 16 km. This resolution is eddy permitting in low and middle latitudes but is too coarse to properly resolve the mesoscale variability in the Arctic region, where the Rossby radius may be as small as 1 – 2 km.

The model is initialized in 1973 using climatology that combines the World Atlas of 2005 (WOA05, Locarnini et al., 2006; Antonov et al., 2006) with version 3.0 of the Polar Science Center Hydrographic Climatology (Steele et al., 2001). At the lateral boundaries,

model fields are relaxed towards the same monthly climatology. The model includes an additional barotropic inflow of 0.7 Sv through the Bering Strait, representing the inflow of Pacific water. A monthly climatology for river discharge is derived by applying run-off estimates from the ERA-Interim product to the Total Runoff Integrating Pathways algorithm (TRIP, Oki and Sud, 1998).

2.2 Data assimilation

The ensemble Kalman filter (EnKF) is a data assimilation method with which the time-dependent state error covariance is computed from a perturbed stochastic ensemble. The method assimilates the data asynchronously (Sakov et al., 2010) in a weekly cycle. An ensemble of 100 members is used here. The analysis is solved in a local framework (Evensen, 2003) with a radius of 300 km, in order to limit long-range spurious correlations introduced by insufficient ensemble rank. Continuity of the update is ensured with a distance-dependent function (Gaspari and Cohn, 1999). A small ensemble inflation is applied by multiplying deviations from the ensemble mean by a factor of 1.01. The ensemble inflation is implemented as a remedy for a tendency of the EnKF to reduce the ensemble spread (Sakov and Oke, 2008). Observation errors are assumed to be uncorrelated.

The EnKF assumes that the variability developed from a perturbed ensemble is representative of the forecast error. This assumption is based on the fact that the model will diverge faster in dynamically chaotic regions. Perturbing model states indirectly through the forcing fields or uncertain model parameter ensures their dynamical consistency. The perturbation system is described in Section 2.4.

The TOPAZ system assimilates the along-track sea level anomalies (SLA) from satellite altimeters from AVISO (asynchronously), sea surface temperature (SST) from the Operational Sea Surface Temperature and Sea Ice Analysis, in situ temperature and salinity profiles from Argo floats, sea ice concentration from AMSR-E, and sea ice drift data from CERSAT. The system uses a 7-day assimilation cycle and assimilates the gridded SST, sea ice concentration, and ice drift fields for the day of the analysis and along-track SLA and *in situ* T and S for the week prior to the analysis.

The data assimilation code is publicly available. It can be accessed from `https://svn.nersc.no/repos/enkf` or browsed at
`https://svn.nersc.no/enkf/browser`.

2.3 Atmospheric forcing

Atmospheric forcing fluxes are derived from a 6-hourly ECMWF product. The surface fluxes are implemented with a bulk formula parametrization (Kara et al., 2000) and the wind stress is derived from 10-m winds, estimated as in Large and Pond (1981).

2.4 Ensemble genesis and perturbation

The model perturbation system accounts for the model error by increasing the model spread through random perturbations of a number of forcing fields. Note that the EnKF is a sequential data assimilation method. During each cycle the ensemble is propagated forward in time, starting from the analysis at the previous cycle. The initial ensemble is created from a historical perturbed ensemble. Following that, the ensemble variability is maintained by perturbing the forcing fields and using ensemble inflation.

The initial ensemble is generated so that it contains variability both in the interior of the ocean and at the surface. We take 20 random model states from each September of a 20-year model run (1990 − 2009). Each state is then used to produce five alternative states by adding spatially correlated noise to the thickness of isopycnal layers and sea ice thickness, with an amplitude that is 10 % of each field, with a spatial decorrelation length scale of 50 km. The perturbation of ocean layer thickness also has a vertical decorrelation scale of three layers and an exponential covariance structure. This ensemble is then spun up during a period of 5 months with perturbation of the forcing, and then the strength of the assimilation is gradually increased over a period of a year.

The perturbations of the forcing fields are assumed to be red noise simulated by the spectral method described by Evensen (2003), computed with a decorrelation timescale of 2 days and decorrelation length scale of 250 km (Brusdal et al., 2003).

Sea level pressure (SLP) is perturbed with a standard deviation of 3.2 hPa. The wind perturbations are the geostrophic winds related to the SLP perturbations, their intensity being inversely proportional to the value of the Coriolis parameter. At 40° N the standard deviations of the winds are 1.5 m/s. In order to account for the absence of geostrophic equilibrium at the equator, the wind perturbations change smoothly from 15° N to the equator, where they are aligned with the gradients of SLP perturbations. In a linear ocean model, such perturbations would add Gaussian random increments to the surface velocities and result in a quasi-Gaussian distribution of drifter positions, though not
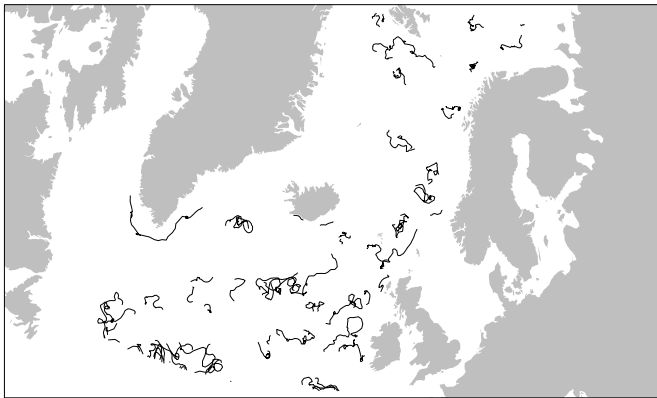
Fig. 1 Trajectories of the 54 surface drifters that are used in the present study. Observations are from the period 2011-06-15 – 2011-07-29, in the Atlantic sector north of 50° N.

exactly Gaussian due the nonlinear Lagrangian trajectory model (Özgökmen et al., 2000).

Further, ensemble member no. 1 is integrated with unperturbed atmospheric forcing. Hence, we will refer to the results from this member as deterministic.

3 Data from drifting buoys

The drifter data come from the archive at the Global Drifter Program. Each drifter consists of a surface buoy, with a transmitter and a subsurface drogue at 15-m depth. Thus, the drifter tracks in principle reflect the currents at 15-m depth, rather than the surface. Most of the buoys are tracked by the Argos satellite system, yielding positions with $150 - 1,000$-m accuracy, up to 20 times per day. The remainder are tracked by GPS, with positional accuracies of 10 m. The ARGOS positions were quality controlled and interpolated via a Kriging method to 6-h intervals at AOML/NOAA (Lumpkin and Pazos, 2007).

The data in the Nordic Seas span the period from 1990 to the present, from over 400 drifters. The drifters have been used previously to analyze the mean surface flow in the region (Poulain et al., 1996; Orvik and Niiler, 2002; Jakobsen et al., 2003; Koszalka et al., 2011) seasonal variability of the currents (Andersson et al., 2011) and mesoscale stirring (Koszalka et al., 2009), among other things. Here, we examine a subset of the data, which is constituted of observations from the Atlantic sector north of 50°N from the period June 15 – July 28, 2011. The trajectories of the 54 drifters in this subset are displayed in Fig. 1.

As the drifters are tracking the 15-m currents, they are influenced by the Ekman (wind-induced) drift, by the geostrophic eddies penetrating to deeper levels and by tides (e.g. Lumpkin and Pazos, 2007 and references

therein). At timescales exceeding a couple of days, the geostrophic current dominate the motion, but the motion at shorter timescales has significant ageostrophic contributions (Rio and Hernandez, 2003). Given the nature of Lagrangian motion, all timescales contribute to a degree to the trajectories, which effectively integrate the velocities in time.

Nevertheless, previous studies suggest that drifter motion can be represented as a superposition of advection by the time mean flow plus a stochastic term which represents the dispersion (e.g. Griffa, 1996; LaCasce, 2008). The most successful models are those in which the perturbed variable is the velocity (rather than the position, as with a random walk), although higher order models (e.g. and McWilliams, 2002) and models with "spin" (et al., 2004) have also been explored.

How sensitive is a drifter trajectory to its initial position? This can be addressed by studying the relative motion of pairs of drifters, launched close to one another. Such a study (of "relative dispersion") was made in the Nordic Seas by Koszalka et al. (2009) and LaCasce (2010). The results suggest that separations between drifters grow exponentially in time, with an e-folding time of roughly a half day. The exponential growth proceeds until the pairs are about 10 km apart, a distance comparable to the deformation radius. Thereafter, the separations grow at a slower rate. When the pairs are 100 km apart on average, the individual motion is uncorrelated.

These results imply that drifter trajectories are sensitively dependent on their initial conditions, as exponential growth is a signature of Lagrangian chaos. Thus, a model has little chance of capturing a drifter trajectory, at least at timescales beyond a couple of days. Nevertheless, since individual trajectories can be modeled stochastically, one would expect the trajectory to fall within the envelope of an ensemble of simulations, provided the dispersion in the modeled fields was similar to that in reality and provided the mean flow was correctly given by the results from the circulation model.

Model results are available as daily mean values centered at noon (all dates are in Coordinated Universal Time). Hence, we split drifter trajectories into daily segments with start and end position interpolated at midnight, as described above. By this method, a total of 1,685 segments from the 54 drifters were available for our analysis.

Expt.	T (h)	trajec.s	memb.s	perturbations		
				no.	p$_0$	u,v
1	24	1685	100	no		
2	48	1651	100	no		
3	72	1614	100	no		
4	24	1685	1	100	yes	no
5	24	1685	1	100	yes	yes

Table 1 List of main sets of trajectory simulations. Columns give information on the following simulation characteristics: **Expt.** is a reference number for each experiment, **T** is the trajectory integration period, **trajec.s** are no. of drifting buoy trajectory segments, **memb.s** is ensemble size (=1 if only the deterministic member or the ensemble mean is used), **perturbations**, if applied, shows no. of perturbations for each trajectory, and if Gaussian noise is being added to the initial position (p$_0$) and/or velocities (u,v). See the text for details.

4 Analysis methods and results

4.1 Drift simulations and a stochastic model

Trajectory simulations are performed as post-processing of the model results, by integration of velocity components using the Runge-Kutta fourth-order method. Daily mean values of the horizontal velocity components are used, with an integration time step of 4 h. Thus, there is one simulated trajectory from the results of each ensemble member.

The trajectory simulation experiments are given in Table 1. In experiments 1, 2, and 3 in Table 1, trajectories are computed for the full 100-member ensemble for drift times of 1, 2, and 3 days, respectively.

Velocities at simulated positions were derived using bi-linear interpolation horizontally. All trajectories were computed from a position at midnight to midnight positions 1, 2, and 3 days later. For each 1 h integration time step, daily mean velocities from the relevant day were used.

We construct a complementary ensemble by 100 perturbations of the initial position prior to integration and using velocities from the deterministic simulation (experiment 4 in the table). This was done in order to quantify the model sensitivity to positioning errors. The perturbations are given by drawing random offsets in both horizontal directions from a Gaussian distribution with a standard deviation of 1 km. This length scale was chosen on the basis that positional errors are 0.15 – 1 km for drifting buoys that are tracked by AR-GOS (recall however that the GPS drifters have much smaller position errors). Note too that the interpolation in time that is performed to produce a synoptic data set also contributes to position errors in our analysis.

Finally, in experiment 5 we examine the results from an alternative model in which the drift is described by perturbing the model velocities. Again, a set of 100 trajectories are used. The velocities here are specified as a first-order stochastic process by

$$(u,v) = (u^f, v^f) + (u', v'), \tag{1}$$

$$(du', dv') = -\kappa(u', v')dt' + v_0\sqrt{2/T_e}dW \tag{2}$$

where u^f and v^f are the velocity components from the deterministic TOPAZ forecast or the ensemble mean forecast and u', v' are perturbations that represent the variability due to unresolved processes in the model. Here, $dt' = 1$ h is the integration time step used for calculating velocity perturbations and $dW = \sqrt{dt'}N(0,1)$ is the incremental Wiener process of a normal distribution (Sawford, 1993). The parameters κ and v_0 determine the behavior of the stochastic component.

In the model, the perturbation velocity has a "memory" of previous values which decays exponentially in time, with e-folding time T_e. The parameter κ then becomes $1 - dt'/T_e$. A reasonable value for T_e is the Lagrangian integral timescale, which is approximately 1 day in the Nordic Seas (e.g. Koszalka et al., 2009; Andersson et al., 2011).

The parameter v_0 determines the rms of the perturbation velocity. One can obtain this by matching moments of the observed dispersion of a set of particles (e.g. Griffa et al., 1995). We chose simply to vary the parameter and compare the resulting dispersion visually with the ensemble dispersion. Using a value of $v_0 = 0.11$ m/s produced comparable dispersion, so we used this value hereafter.

Ideally, one would use stochastic perturbations for each ensemble member in order to account for unresolved processes. From a relativistic perspective, the resulting inflation will be larger for smaller convex hulls.

4.2 Validation methods

The main purpose of this study is to compare using a single forecast of a drifter position to using an ensemble. As the motion of a single drifter is in principle unpredictable, the average position of a group of trajectories may be more valuable than a single calculated trajectory. A straightforward method to quantify the difference in the two approaches is to compare the distances from the observed buoy position to that of the deterministic position and to that of the ensemble forecast's center of gravity (CoG, i.e. the mean position). These two distances are indicated by the dark green line and the dark gray line in Fig. 2.

The ensemble spread will be represented by the convex hull of all ensemble members, defined as the closed curve which connects the outermost members and contains all the other members. It is illustrated by the blue

line in Fig. 2. The monotone chain algorithm due to Andrew (1979) was used for determining the convex hull. The convex hull area increases with the ensemble size n, but rather slowly (in $O(\sqrt{\log(n)})$ for Gaussian points) Rényi and Sulanke (1963), which makes it well suited to the small ensemble sizes used in operational settings.

Counting the number of observed buoy positions that fall inside and outside of the convex hulls provides information on the accuracy of the ensemble forecast. However, such results are not sufficient to establish our results as a valid representation of the stochastic variability, since, e.g., all observations would occur inside a sufficiently inflated convex hull. In order to gain more insight into the ensemble forecast, we will also examine relations between the area of the hull and the distance between the observations and the ensemble CoG.

4.3 Validation results

Positions of all drifting buoy locations that are validated in this study are displayed in Fig. 3. Locations
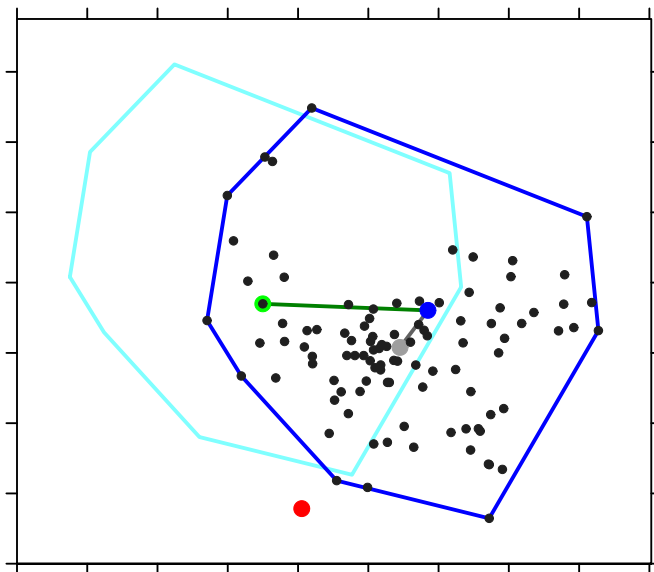

Fig. 2 Validation metrics illustration. Shown here are results from 1 day drift observations and simulations. The initial position is given by the red marker, and the buoy position 24 hours later is displayed by the blue marker. The end points of the integration of all 100 ensemble members are given by the small black markers, the position of the deterministic simulation (member 1) is plotted on top of a green marker. The center of gravity (CoG) of the ensemble results are shown by the gray marker, and a blue line marks the perimeter of the convex hull of the ensemble results. The convex hull, as it would appear with its shape retained if the CoG was shifted to the result from the deterministic simulation is indicated by the light blue line. The distance from the observed buoy position after the 24-h drift to the positions of the deterministic forecast, and to the ensemble CoG are displayed by the dark green and dark gray lines, respectively. Tick lines on the x- and y-axes are drawn for every 5 km.

Observations inside polygon
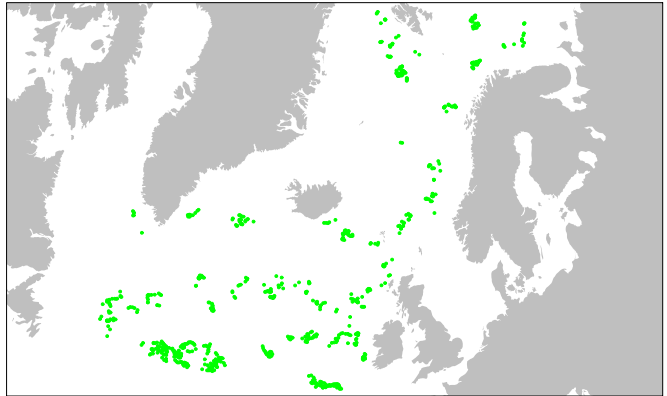
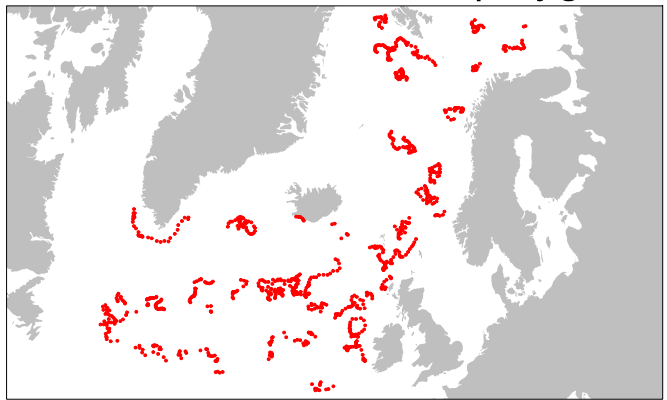## Observations outside polygon

Fig. 3 Maps displaying drifting buoy positions where observations of 24-h drift fall inside the ensemble convex hull (top panel, green markers) and outside the convex hull (bottom panel, red markers) for experiment 1.

where observations of 24-h drift fall inside and outside of the convex hulls in experiment 1 are displayed in the top and bottom panel, respectively. Hereafter, convex hulls that contain the end point of the relevant trajectory segment are referred to as a "hits", while hulls that do not cover the end point are referred to as "misses". The results from experiment 1 reveal a hit rate of 0.45 (see Table 2).

We find that the hull areas are much larger for hits than for misses, with average values of $1{,}280\,\mathrm{km^2}$ and $410\,\mathrm{km^2}$, respectively. This may be an indication that hits occur for the simple reason that the corresponding hulls are inflated to the degree that their sheer size makes it more likely that hits are recorded. However, when we inspect the distances from the convex hulls' CoG to the observed positions, we find that the average distance for hits is $10.4\,\mathrm{km}$. This corresponds to a circular domain of about $350\,\mathrm{km^2}$, markedly smaller than the average convex hull area in these cases ($1{,}280\,\mathrm{km^2}$).

Hence, hits generally occur well inside the convex hulls, as is the case with the sample forecast displayed

in Fig. 2. Similar results are found for 48-h drift and 72-h drift (experiments 2 and 3), and we note that the observation-to-CoG distance increases slower than linearly in time.

An obvious alternative to the convex hull approach is to define a circular search area centered at the ensemble CoG (or the deterministic forecast). Hence, we computed how large such an area must be in order to arrive at the same frequency of hits as with the convex hulls. The results, given in the row labeled "equivalent circle area" reveals that for the ensemble-based 24-h drift simulations (experiment 1, 1^{circ}, 5^{ens}) this area becomes larger as frequency of hits increases, as expected. Furthermore, as noted above, most of the hits recorded from experiment 1 occur well inside the convex hulls, making a circular search area a more efficient choice.

Next, we use offsets of simulated trajectories relative to observations to compare predictions using the CoG of the forecast ensemble with predictions using a single deterministic forecast. We first note that for hits, the average offsets for 24-h drift in these two cases are 10.4 and 13.7 km, respectively (see Table 2). The definition of a hit will favor CoG results since the ensemble results that define the CoG also define the perimeter of the convex hull. Still, we infer that the CoG is a more precise forecast than the traditional deterministic fore-cast, for two reasons. From Table 2 the CoGs are closer to the observations also for misses. This can also be seen in Fig. 4, where the misses are largely found near the diagonal.

Second, we attempt to skew the probabilities to favor the deterministic forecast by shifting the convex hulls' centers from the CoG to the deterministic forecast. When we record the hits for the shifted convex hulls, we find that the offsets are about the same for the deterministic forecast hits (10.3 km) as for the CoG hits (10.4 km).

Initial perturbations corresponding to drifter positioning errors of O(1 km) contribute little to trajectory variability, yielding a very low hit rate for the convex hulls when the perturbations are applied in deterministic simulations (experiment 4 in Table 1). Thus, our results are not very sensitive to small errors in the trajectory initialization. However, the lack of variability found in experiment 4 is unsurprising, since the perturbation distances are smaller than the model resolution by an order of magnitude and smaller still than the features that are resolved by TOPAZ.

Variability is also likely to be restrained by the use of daily mean values. Dispersion due to actions of surface gravity waves is not modeled, but the effect of this shortcoming is expected to be low since the buoys we consider mainly drift with the drogue at 15-m depth.

		Experiment no.					
	1	1^{circ}	**2**	**3**	**4**	5^{det}	5^{ens}
	Frequency, observation inside polygon						
	0.45	0.40	0.47	0.49	0.04	0.53	0.56
	Average polygon area (km^2)						
observation inside polygon	1280	1380	3740	6410	18	560	560
observation outside polygon	410	400	1500	3070	17	550	540
all observations	800		2550	4700	17	550	550
equivalent circle area	400	340	1480	3030	23	760	750
	Average ensemble offset (km)						
observation inside polygon	10.4	10.1	18.6	25.1	N/A	N/A	10.7
observation outside polygon	18.5	18.2	34.7	49.3	N/A	N/A	24.8
all observations	14.9		27.2	37.5	N/A	N/A	16.9
	Average deterministic offset (km)						
observation inside polygon	13.7	14.2	24.6	33.0	2.1	10.7	N/A
observation outside polygon	19.2	18.5	35.8	50.9	17.4	27.4	N/A
all observations	16.7		30.6	42.2	16.8	18.5	N/A
	Computational cost						
	1	1	2	3	0.8	0.8	0.8

Table 2 Results from experiments with simulation of drifting buoy trajectories. Experiment numbers refer to the list in Table 1. Results under experiment 1^{circ} were obtained by replacing all convex hulls by a circular target area with of the same size as the corresponding convex hull. Differences between experiment 5^{det} and 5^{ens} arise from advecting drifters by the results from member 1 and the ensemble mean, respectively. "Polygon" refers to the convex hull of the ensemble forecast, as described in Section 4.2. Results in the table row "equivalent circle area" correspond to the area of an invariant circle, centered at the center of gravity (CoG), which gives the same frequency of hits as reported in the top row. Moreover, "ensemble offset" is the distance from the observed position of the drifting buoy to the ensemble CoG at the end of the simulation, while "deterministic offset" is the corresponding distance to the result from the deterministic forecast (member 1). The computational cost is given relative to the resources required for experiment 1. *N/A* not applicable
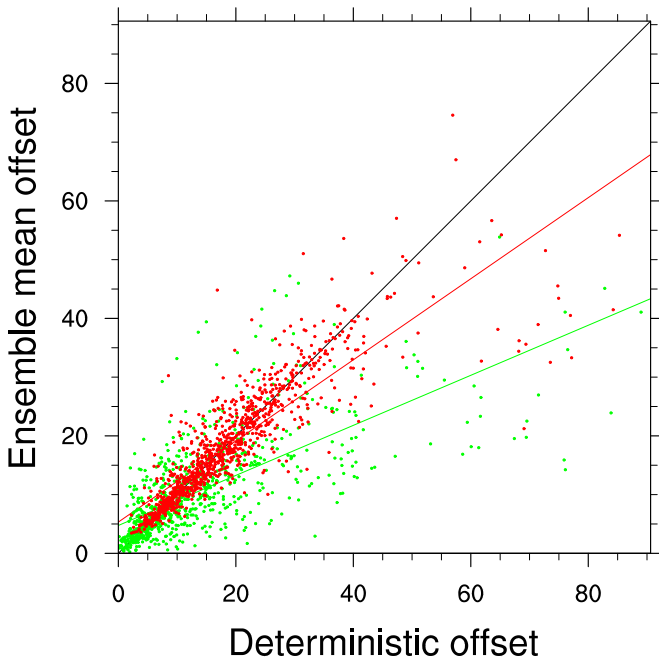
Fig. 4 Scatter plot that depicts the distance between the end point of the drifting buoy trajectory and two forecasts. The distance to the deterministic forecast is given by the x-axis, while the distance to the ensemble center of gravity is given by the y-axis. Green and red markers correspond to cases where the trajectory is inside and outside of the ensemble's convex hull, respectively. Least squares fit to the results for trajectories that fall inside and outside of the hull are displayed by the green and red line, respectively. Values along the axes are distances in km.

Moreover, the present implementation of TOPAZ does not include tidal motion. Even though we examine drift for periods that are close to multiples of the main tidal constituents, this shortcoming will affect our results. Nevertheless, most of the drifter data used in the present validation are recorded in deep waters where the tidal currents are of less significance than on the continental shelf. Hence, the statistics in Table 2 may not be representative for coastal waters.

Experiment 5 is the alternative stochastic model that was described in Section 4.1, where the velocity components are perturbed. We consider results obtained by perturbing the deterministic velocity forecast (5^{det}), and by perturbing the ensemble mean forecast (5^{ens}). The resulting convex hulls are of similar magnitude as in experiment 1, by design (we chose v_0 in order to roughly replicate the observed dispersion). The hit rates from the two variants of experiment 5 become 0.53 and 0.56, which are a significant improvement over the ensemble model in experiment 1.

Moreover, although the velocity perturbations in experiment 5 have the same magnitude for all trajectory simulations, the areas of the resulting hulls vary between 340 and 880 km^2. This distribution is due to

variations in divergence/convergence of the background currents (u^f, v^f in Eq. 1). Since the search area in experiment 5 is markedly smaller than the equivalent circle area, we infer that the velocity perturbation algorithm is a valuable approach to confine the search area.

Finally, we consider the results from experiment 1^{circ}, where the analysis is repeated after replacing each convex hull from experiment 1 by a circle of the same area as the hull. The hit rate drops somewhat (to 0.40), suggesting that the geometrical distribution of the ensemble results, as represented by the convex hulls, contains information. Further, in 26 % of the cases, both the observed position and the buoy's initial position were inside of the circle. As an alternative, we repositioned the circles so that their centers were set to the initial position of the trajectory segment. We found that this led to a very marginal drop in the hit frequency, to 0.39.

The probability density function of the displacements about the CoG for the ensemble can reasonably be fit with a Rayleigh distribution, implying that the separation of the observed buoy from the CoG can be assessed using standard statistical measures. Thus, on average, 1.1 and 5.3 % of the ensemble members fall outside of the 99 and 95 % confidence intervals from the Rayleigh distribution, respectively. Further investigations reveal that the 24-h drift hit ratio from experiment 1 of 0.45 with convex hulls corresponds to applying a 92 % confidence interval with the Rayleigh distribution.

The model results we use are the model representation of currents in the uppermost 3 m of the water column. As pointed out in Section 3 the drifters have a drogue at 15-m depth. Ensemble results are not available at this level, but the ensemble mean field (i.e., averaging in ensemble member space) has been stored for all model layers. We compute the temporal average ratio between the current speed at the two levels and the corresponding average deflection angle between the levels, from ensemble mean results for June and July (deflection angles were weighed by the speed). Time invariant velocity modification fields were thus available with the same spatial resolution as the ensemble product. The trajectory simulations in experiment 1 are repeated, but with speeds and angles modified in compliance with this algorithm. However, we find that the performance deteriorates when compared to the results from experiment 1, we, e.g., get a hit rate of only 0.28. Generally, the model currents at 15-m depth are somewhat weaker that at 3 m, so drift distances will be shorter.

From Fig. 5a, we find that the frequency distribution the 24-h Lagrangian drift with model currents is skewed towards short distances between start and end
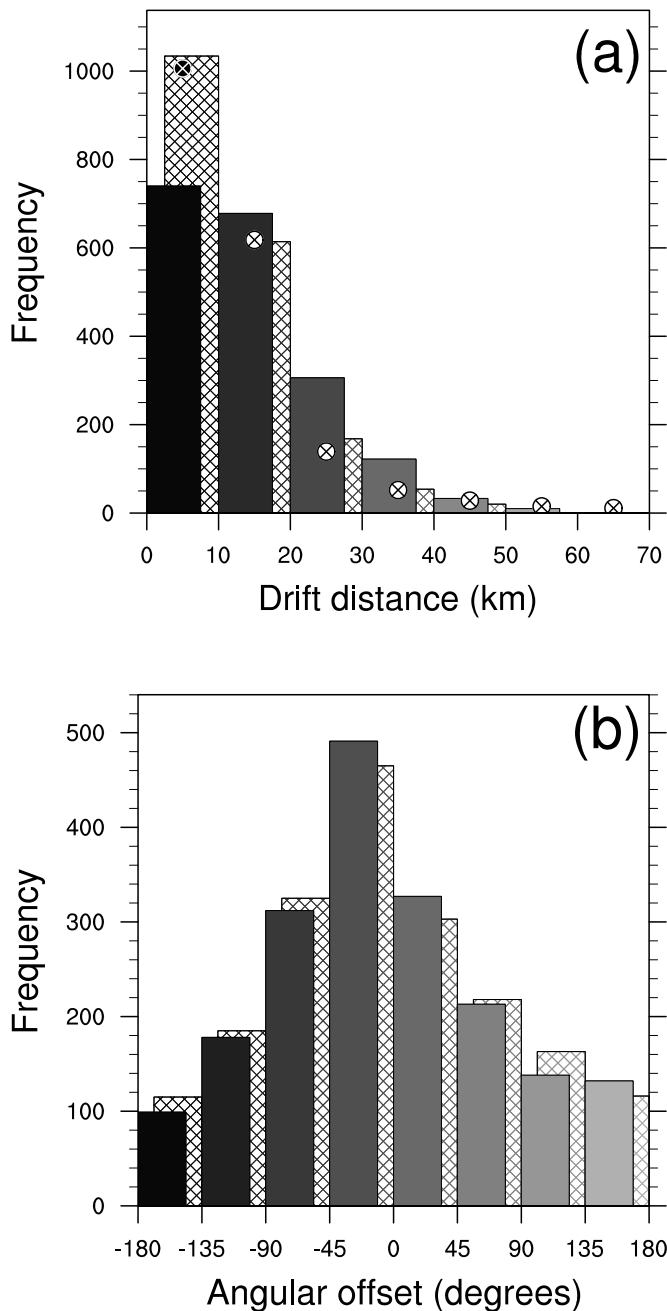
Fig. 5 (a) Distribution of separation between drifter position at initial time, and the position 24 h later. The results from 1,685 trajectories are counted in bins of 10 km. Bin limits and no. of trajectories in each bin are given by the x and y axis, respectively. The filled vertical bars correspond to data from observations, the hatched bars show the center of gravity results, and $\otimes$ marks results from the corresponding deterministic simulations. Note that the trajectory count from the deterministic run for the two rightmost bins is 14 and 10, respectively. (b) Angular offsets in the trajectory paths between results from observations and center of gravity (filled bars), and between observations and the deterministic trajectories (hatched bars). Positive values correspond to model results veering to the left of the observed trajectories.

points of the trajectories, as one should expect with a model that is not eddy resolving. This explains why the quality of trajectory simulations with model currents at 15-m depth is worse than when calculated from the surface currents (experiment 1). Moreover, the angular offsets in Fig. 5b reveal that the model results are shifted somewhat to the right of the observations, while the wind-driven current near the surface is shifted to the left of its direction at deeper levels in the northern hemisphere. Since the parameterization of surface momentum fluxes has not been fine-tuned in the model, and since the current at 3-m depth yields better fits to the drifter data, we use the results from 3-m depth in this study.

We recall from Section 2 that the model results are available on the basis of a weekly cycle. In Fig. 6, the average area of the convex hulls is displayed as a function of time after the assimilation step in the TOPAZ production. We observe that the hull areas grow with the forecast time range. This reflects the evolution that is expected in a turbulent flow, where differences between ensemble members grow in time.

We also note from Fig. 6 that there is no obvious relation between hull areas and hit rates in the context of variations during the weekly TOPAZ cycle. The drifting buoys have knowledge of neither the TOPAZ system nor the day of the week. Further, the atmospheric forcing in the present weekly cycle is approximately homogeneous. Hence, we suspect that even though the hull
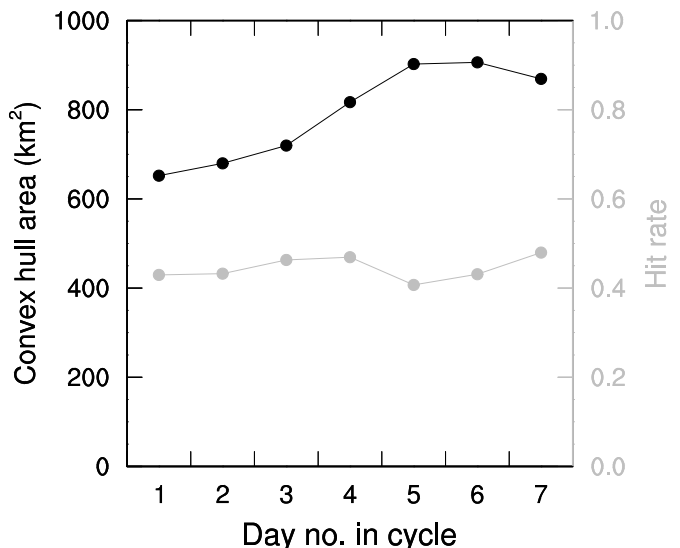

Fig. 6 Changes in average convex hull area and hit rate as a function of day in the weekly TOPAZ cycle. Day 1 and day 7 results represent the first 24 h after assimilation and the final 24 hours before the next assimilation step. The results for hull areas are displayed by the black markers, with values given at the left y-axis, while hit rates are displayed by gray markers with values at the right y-axis.

areas grow with forecast time range, i.e., reducing the precision of the forecast, the accuracy is also reduced with forecast time range since the hit rate does not increase.

In order to examine effects of the variability in the surface kinetic energy density ($E_k = (u^2 + v^2)/2$), we first partition this quantity locally by writing

$$E_k(x, y, t, m) = \overline{E_k}(x, y) + \hat{E}_k(x, y, t)$$
$$+ E'_k(x, y, t, m) \qquad (3)$$

where m denotes ensemble member. Here, $\overline{E_k}$, $\hat{E}_k$, and E'_k denote the overall mean value in time and ensemble space, the difference between the (time-dependent) ensemble mean and $\overline{E_k}$, and the difference between each ensemble member and $\hat{E}_k$, respectively. We next introduce the fraction of variability due to the ensemble variance to the total variability, which we may write

$$< E'^{\,2}_k > / < (E_k - \overline{E_k})^2 > \qquad (4)$$

Here, angled brackets indicate the ensemble average value. This quantity is properly referred to as the fraction of nondeterministic variability, see Metzger and Hurlburt (2001) and Melsom (2005) for details.

The time average of the fraction of nondeterministic variability of the kinetic energy density is displayed in Fig. 7. We note that the ensemble variance dominates in dynamically active regions.

Mean convex hull areas during each weekly TOPAZ production cycle (Section 2) were computed separately for each drifter, by averaging the hull areas that correspond to available trajectory segments for this drifter (the average thus represent between one and seven segments, depending on availability of data). Results for the ensemble-based simulation of 24-h drift are overlaid in Fig. 7. As expected, the convex hulls generally become large in regions of high nondeterministic variability. But note that this quantity is an expression for relative, not absolute, variability.

The set of available trajectories, shown in Fig. 1, is sparse and not distributed uniformly over the domain. So our results should not be interpreted as being general for the present domain. In this perspective, the regional differences displayed in Fig. 7 give valuable information regarding the clustering of relatively small and large convex hulls in relation to the local flow regime.

Above, we achieved a higher hit rate when the stochastic model was applied to the deterministic model results in experiment 5^{det} than in the ensemble results from experiment 1. On the other hand, we found that the ensemble CoG is generally closer to the observed buoy positions than the deterministic result (ensemble member no. 1).
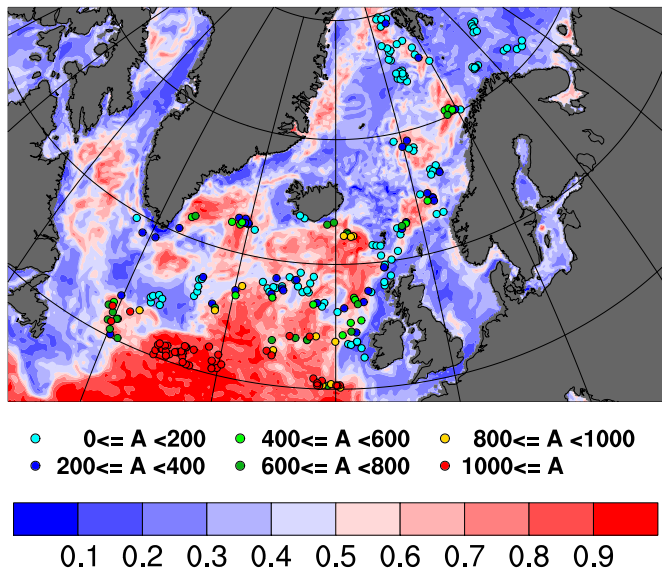

Fig. 7 Fraction of nondeterministic variability in the model results for kinetic energy density in the uppermost layer. Only the subdomain from which trajectories are studied is displayed here. The color coding of the fraction values is given by the color bar. Superimposed on this are weekly average convex hull areas, presented as filled and colored circles. The corresponding color coding is displayed by the labeled circles. See the text for details.

These results may appear contradictory, but they are due to the nonsymmetric distribution of convex hull areas from experiment 1 that is displayed by the black line in Fig. 8. More than 60 % of the convex hulls from experiment 1 have an area of 400 km^2 or less (nearly 50 % have an area $<$200 km^2). For these area slots, the hit frequency in experiment 1 is about 0.3 only.

On the other hand, the stochastic model (using $v_0 = 0.11$ m/s) inflates hull areas in regions with low ensemble variability, thus recording significantly more hits in such regions. Relevant examples for these cases are found, e.g., in the northern Nordic Seas and off the southern tip of Iceland, where low ensemble variability and small hull areas (Fig. 7) are seen in regions where the hit-to-miss ratio is low (Fig. 3).

5 Discussion

We have described the initial implementation of a probabilistic forecast, but there are several ways it could be enhanced: first by adjusting the horizontal radius and timescale of the perturbations of atmospheric forcing fields, then by fine-tuning the air – sea momentum fluxes by for example taking into account the influence of waves on the mixing. We also expect that the results will improve with model resolution. Then, given sufficient density of observations, the impact of data as-

simulation will be more visible in the evolution of the hit rate during the weekly cycle.

In search and rescue operations, it is of crucial importance to have a search area which is "small" and yet have a high probability of retrieving the lost object. The results displayed in Fig. 8 reveal that search areas are frequently underestimated by the convex hulls that span the ensemble trajectories.

Nevertheless, the stochastic experiment gives hit frequencies of about $0.15 - 0.25$ only when the convex hull areas from the ensemble experiment exceed $2,000\,\mathrm{km}^2$. This suggests that the ensemble dispersion reflects an increasing uncertainty in the end positions of trajectories in regions where the relevant ocean circulation processes give rise to high dispersion rates. In the domain that is examined here, such large convex hull areas are only found south of $55°\,\mathrm{N}$ (see Fig. 7).

In an operational setting, other elements may also be fine-tuned on the basis of validation results. As an example, drift velocities from model results may be increased systematically in order to compensate for the bias that can be seen in Fig. 5. Formulations that in-
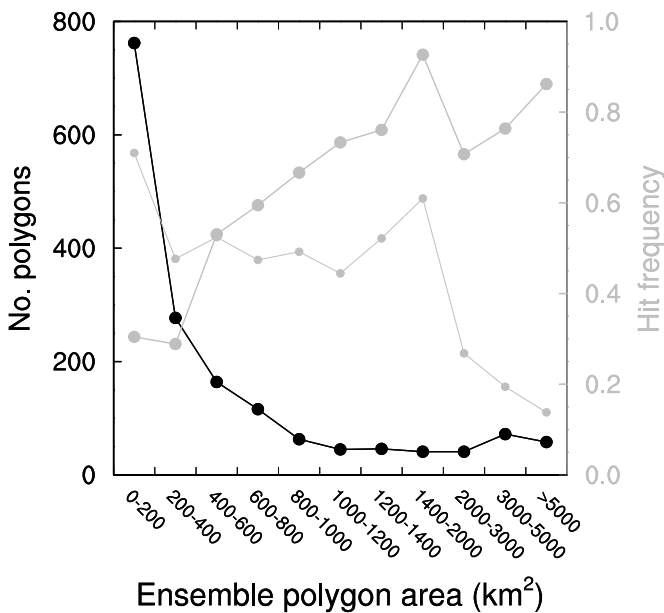
volve the statistical moments of the ensemble distribution may provide useful and condensed information about the results.

We conclude that among the various approaches to drift modeling that we have tested, the best drift forecasts will be achieved by expanding the search areas beyond the convex hulls based on ensemble trajectories when this area is of modest size. If, on the other hand, the convex hull area is large, a search and rescue effort should anticipate that a wider area must be covered in order to recover the lost object. In this context, the limits for when the convex hulls are "large" and "small" are likely to depend on the horizontal resolution of the ocean circulation model.

It is particularly noteworthy that all results improve when the deterministic results are substituted by the ensemble mean values. Moreover, shifting to more frequent assimilation steps is likely to be beneficial for the quality of the ensemble trajectory forecast from TOPAZ.

Fig. 8 Comparison of results from the ensemble experiment and the stochastic perturbation experiment (expt. 1 and 5^{ens} in Table 1, respectively). Results are displayed as functions of polygon area from the ensemble experiment. Black line and markers show no. of polygons recorded in each of the area intervals that are listed along the x-axis. Thick gray line and large gray markers show the distribution of hit frequencies from the ensemble experiment. Thin gray line and small gray markers show the corresponding distribution from the stochastic experiment. Note that the hit frequency distribution by polygon area slots for the stochastic experiment was computed as a function of the ensemble experiment area of the corresponding observed trajectory (and thus not the stochastic experiment polygon area).

References

Allen, A. A. and J. V. Plourde, Review of leeway: field experiments and implementation. USCG RD center technical report CG-D-08-99. (1999)

Andersson, M., J. H. LaCasce, K. J. Orvik, I. Koszalka and C. Mauritzen, Variability of the Norwegian Atlantic Current and associated eddy field from surface drifters. *J. Geophys. Res.*, **116**, C08032, 16 pp. (2011) doi:10.1029/2011JC007078

Andrew, A. T., Another Efficient Algorithm for Convex Hulls in Two Dimensions. *Info. Proc. Lett.*, **9**, 216-219 (1979)

Antonov, J. I., R. A. Locarnini, T. P. Boyer, A. V. Mishonov and H. E. Garcia, World Ocean Atlas 2005, Volume 2: Salinity. S. Levitus, Ed. NOAA Atlas NESDIS **62**, U.S. Government Printing Office, Washington, D.C., 182 pp. (2006)

Berloff, P. S. and J. C. McWilliams, Material Transport in Oceanic Gyres. Part II: Hierarchy of Stochastic Models. *J. Phys. Oceanogr.*, **32**, 797-830 (2002)

Bertino, L. and K. A. Lisæter, The TOPAZ monitoring and prediction system for the Atlantic and Arctic Oceans. *J. Oper. Oceanogr.*, **1**(2), 1518 (2008)

Bleck, R., An oceanic general circulation model framed in hybrid isopycnic-cartesian coordinates. *Ocean Model.*, **4**, 55-88 (2002)

Breivik Ø. and A. A. Allen, An operational search and rescue model for the Norwegian Sea and the North Sea. *J. Mar. Sys.*, **69**, 99-113 (2008) doi:10.1016/j.jmarsys.2007.02.010

Breivik, Ø., A. A. Allen, C. Maisondieu and J. C. Roth, Wind-induced drift of objects at sea: The leeway field method. *Appl. Ocean Res.*, **33**, 100-109 (2011) doi:10.1016/j.apor.2011.01.005

Brusdal, K., J. Brankart, G. Halberstadt, G. Evensen, P. Brasseur, P. J. van Leeuwen, E. Dombrowsky and J. Verron, An evaluation of ensemble based assimilation methods with a layered OGCM. *J. Mar. Sys.*, **40-41**, 253-289 (2003)

Canuto, V., A. Howard, Y. Cheng and M. Dubovikov, Ocean turbulence. Part II: Vertical diffusivities of momentum, heat, salt, mass, and passive scalars. *J. Phys. Oceanogr.*, **32**, 240-264 (2002) doi:10.1175/1520-0485(2002)032<0240:OTPIVD>2.0.CO;2

Chassignet, E., H. E. Hurlburt, O. M. Smedstad, G. Halliwell, P. Hogan, A. Wallcraft and R. Bleck, Ocean prediction with the hybrid coordinate ocean model (HYCOM). *Ocean Weather Forecasting*, 413-426 (2006)

Evensen, G., Sequential data assimilation with a nonlinear quasi-geostrophic model using Monte-Carlo methods to forecast error statistics. *J. Geophys. Res.*, **99**(C5), 10143-10162 (1994)

Evensen, G., The ensemble Kalman filter: Theoretical formulation and practical implementation. *Ocean Dyn.* **53**, 343-367 (2003) doi:10.1007/s10236-003-0036-9

Gaspari, G. and S. E. Cohn, Construction of correlation functions in two and three dimension. *Q. J. R. Meteorol. Soc.*, **125**, 723-777 (1999)

Griffa, A., Applications of stochastic particle models to oceanographic problems. In Adler et al., eds., *Stochastic Modelling in Physical Oceanography*, Birkhäuser Boston, pp. 113-140 (1996)

Griffa, A., K. Owens, L. Piterbarg and B. Rozovskii, Estimates of turbulence parameters from Lagrangian data using a stochastic particle model. *J. Mar. Res.*, **53**, 371401 (1995)

Hackett, B., Ø Breivik, C. Wettre, C. Forecasting the drift of objects and substances in the oceans. In: Chassignet, Verron, eds., *Ocean Weather Forecasting: An Integrated View of Oceanography*. Springer, pp. 507524 (2006)

Hunke, E. C. and J. K. Dukowicz, An elastic-viscous-plastic model for sea ice dynamics. *J. Phys. Oceanogr.*, **27**, 1849-1867 (1997)

Iskandarani, M., J. Levin, B. Choi and D. Haidvogel, Comparison of advection schemes for high-order hp finite element and finite volume methods. *Ocean Mod.*, **10**(1-2), 233-252 (2005) doi:10.1016/j.ocemod.2004.09.005

Jakobsen, P. K., M. H. Rikergaard, D. Quadfasel, T. Schmith and C. W. Hughes, The near surface circulation in the Northern North Atlantic as inferred from Lagrangian drifters: variability from the mesoscale to interannual. *J. Geophys. Res.*, **108**, 3251, 14 pp. (2003) doi:10.1029/2002JC001554

Kara, A. B., P. A. Rochford and H. E. Hurlburt, Efficient and accurate bulk parameterizations of air-sea fluxes for use in general circulation models. *J. Atmos. Oc. Tech.*, **17**, 1421-1438 (2000)

Koszalka, I., J. H. LaCasce, M. Andersson, K. J. Orvik and C. Mauritzen, Surface circulation in the Nordic Seas from clustered drifters. *Deep Sea Res. I*, **58**(4), 468-485 (2011) doi:10.1016/j.dsr.2011.01.007

Koszalka, I., J. H. LaCasce and K. J. Orvik, Relative dispersion in the Nordic Seas. *J. Mar. Res.* **67**, 411-433 (2009) doi:10.1357/002224009790741102

LaCasce, J. H., Statistics from Lagrangian observations. *Prog. Oceanogr.* **77**, 1-29 (2008)

LaCasce, J. H., Relative displacement PDFs from balloons and drifters. *J. Mar. Res.* **68**, 433-457 (2010) doi:10.1357/002224010794657155

Large, W. G. and S. Pond, Open ocean momentum flux measurements in moderate to strong winds. *J. Phys. Oceanogr.* **11**, 324-336 (1981)

Locarnini, R. A., A. V. Mishonov J. I. Antonov, T. P. Boyer and H. E. Garcia, World Ocean Atlas 2005, Volume 1: Temperature. S. Levitus, Ed. NOAA Atlas NESDIS **61**, U.S. Government Printing Office, Washington, D.C., 182 pp. (2006)

Lumpkin., R. and M. Pazos, Measuring surface currents with Surface Velocity Program drifters: the instrument, its data, and some recent results. In: Griffa et al., eds., *Lagrangian Analysis and Prediction of Coastal and Ocean Dynamics*, Cambridge University Press, pp. 39-67 (2007)

Melsom, A., Mesoscale activity in the North Sea as seen in ensemble simulations. *Ocean Dyn.*, **55**, 338350 (2005) doi:10.1007/s10236-005-0016-3

Melsom, A., Validation of an ocean model ensemble. In: Coastal to global operational oceanography: Achievements and Challenges. Eds.: Dahlin, Bell, Flemming, Petersson. *EuroGOOS publication no. 28*, SMHI, Norrköping, Sweden. pp. 253-259 (2010)

Metzger, E. J. and H. E. Hurlburt, The nondeterministic nature of Kuroshio penetration and eddy shedding in the South China Sea. *J. Phys. Oceanogr.* **31**, 1712-1732 (2001) doi:10.1175/1520-0485(2001)031<1712:TNNOKP>2.0.CO;2

Oki, T. and Y. C. Sud, Design of the global river channel network for Total Runoff Integrating Pathways (TRIP). *Earth Int.* **2** 2-001, 37 pp (1998)

Orvik, K. A. and P. P. Niiler, Major pathways of Atlantic Water in the northern North Atlantic and Nordic Seas towards Arctic. *Geophys. Res. Lett,*, **29**, 1896, 4 pp. (2002) doi:10.1029/2002GL015002

Özgökmen, T. M., A. Griffa, L. I. Piterbarg, and A. J. Mariano, On the predictability of the Lagrangian trajectories in the ocean. *J. Atmos. Ocean. Tech.*, **17**(3), 366-383 (2000)

Poulain, P. M., A. Warn-Varnas and P. P. Niiler, Near-surface circulation of the Nordic Seas as measured by Lagrangian drifters. *J. Geophys. Res.*, **101**, 18237-18258 (1996)

Rényi, A. and R. Sulanke, Über die convexe Hülle von *n* zufällig gewählten Punkten. *Z. Wahr.*, **2**, 75-84 (1963)

Rio, M.-H. and F. Hernandez, High-frequency response of wind-driven currents measured by drifting buoys and altimetry over the world ocean. *J. Geophys. Res.*, **108**, 3283, 19 pp. (2003) doi:10.1029/2002JC001655

Sakov, P., F. Counillon, L. Bertino, P. R. Oke, K. A. Lisæter and A. Korablev, The TOPAZ4 Pilot Reanalysis (2003-2008). *Ocean Science*, submitted (2012)

Sakov, P., G. Evensen and L. Bertino, Asynchronous data assimilation with the EnKF. *Tellus*, **62**A, 24-29 (2010) doi:10.1111/j.1600-0870.2009.00417.x

Sakov, P., P. R. Oke, A deterministic formulation of the ensemble Kalman filter: an alternative to ensemble square root filters. *Tellus*, **60**A, 361-371 (2008) doi:10.1111/j.1600-0870.2007.00299.x

Sawford, B. L., Recent developments in the Lagrangian stochastic theory of turbulent dispersion. *Boundary Layer Meteor.*, **62**, 197215 (1993)

Steele, M., R. Morley and W. Ermold, PHC: A global ocean hydrography with a high-quality Arctic Ocean. *J. Clim.*, **14**, 2079-2087 (2001)

Veneziani M., A. Griffa, A. M. Reynolds and A. J. Mariano, Oceanic turbulence and stochastic models from subsurface Lagrangian data for the North-West Atlantic Ocean. *J. Phys. Oceanogr.*, **34**, 1884-1906 (2004) doi:10.1175/1520-0485(2004)034<1884:OTASMF>2.0.CO;2

Zalesak, S., Fully multidimensional flux-corrected transport algorithms for fluids. *J. Comp. Phys.*, **31**, 335-362 (1979)